

# Silicon Radical-Induced CH<sub>4</sub> Dissociation for Uniform Graphene Coating on Silica Surface

Kritin Pirabul, Qi Zhao, Zheng-Ze Pan,\* Hongyu Liu, Mutsuhiro Itoh, Kenichi Izawa, Makoto Kawai, Rachel Crespo-Otero, Devis Di Tommaso,\* and Hiroto Nishihara\*

Due to the manufacturability of highly well-defined structures and wide-range versatility in its microstructure, SiO<sub>2</sub> is an attractive template for synthesizing graphene frameworks with the desired pore structure. However, its intrinsic inertness constrains the graphene formation via methane chemical vapor deposition. This work overcomes this challenge by successfully achieving uniform graphene coating on a trimethylsilyl-modified SiO<sub>2</sub> (denote TMS-MPS). Remarkably, the onset temperature for graphene growth dropped to 720 °C for the TMS-MPS, as compared to the 885 °C of the pristine SiO<sub>2</sub>. This is found to be mainly from the Si radicals formed from the decomposition of the surface TMS groups. Both experimental and computational results suggest a strong catalytic effect of the Si radicals on the CH<sub>4</sub> dissociation. The surface engineering of SiO<sub>2</sub> templates facilitates the synthesis of high-quality graphene sheets. As a result, the graphene-coated SiO<sub>2</sub> composite exhibits a high electrical conductivity of 0.25 S cm<sup>-1</sup>. Moreover, the removal of the TMS-MPS template has released a graphene framework that replicates the parental TMS-MPS template on both micro- and nano- scales. This study provides tremendous insights into graphene growth chemistries as well as establishes a promising methodology for synthesizing graphene-based materials with pre-designed microstructures and porosity.

integrated with a porous structure, they exhibit highly developed porosity and become suitable for a wide range of practical applications, e.g., in fuel cells,<sup>[2]</sup> supercapacitors,<sup>[3]</sup> lithium–sulfur batteries,<sup>[4]</sup> lithium–oxygen batteries,<sup>[5]</sup> co-photocatalysts,<sup>[6]</sup> catalyst supports,<sup>[7]</sup> and new types of heat pumps.<sup>[8]</sup> So far, porous graphene-based materials have been synthesized by various methods, such as hard templating,<sup>[9]</sup> sugar-blowing technique,<sup>[10]</sup> and graphene oxide assembly.<sup>[11]</sup> Among these, hard templating is promising from the perspective of structural variety because it can potentially use various nanostructured materials as templates.<sup>[12]</sup> It typically uses an inorganic material as a scaffold, and the replicated carbon materials are obtained after template removal.

Synthesis of graphene-based materials using hard templating involves carbon deposition onto the surface of the template. Transition metals such as Ni and Cu are popularly used as hard templates. Chemical vapor deposition (CVD) serves as an effective measure to create a carbon layer via the


decomposition of a volatile carbon precursor. This approach generally consists of four continuous steps: i) transportation and adsorption of precursor molecules on the template; ii) decomposition/dehydrogenation of precursor molecules to form active carbon species; iii) formation of graphene nuclei from the

## 1. Introduction

Graphene-based frameworks have garnered significant attention over the past decade due to their unique electrical, thermal, mechanical, and optical properties.<sup>[1]</sup> When these frameworks are

K. Pirabul, H. Liu, H. Nishihara  
Institute of Multidisciplinary Research for Advanced Materials  
Tohoku University  
2-1-1 Katahira, Aoba-ku, Sendai, Miyagi 980-8577, Japan  
E-mail: hirotomo.nishihara.b1@tohoku.ac.jp

Q. Zhao, D. Di Tommaso  
Department of Chemistry  
Queen Mary University of London  
Mile End Road, London E1 4NS, UK  
E-mail: d.ditomaso@qmul.ac.uk

 The ORCID identification number(s) for the author(s) of this article can be found under <https://doi.org/10.1002/smll.202306325>

© 2023 The Authors. Small published by Wiley-VCH GmbH. This is an open access article under the terms of the Creative Commons Attribution License, which permits use, distribution and reproduction in any medium, provided the original work is properly cited.

DOI: 10.1002/smll.202306325

Z.-Z. Pan, H. Nishihara  
Advanced Institute for Materials Research (WPI-AIMR)  
Tohoku University  
2-1-1 Katahira, Aoba-ku, Sendai, Miyagi 980-8577, Japan  
E-mail: pan.zhengze.e6@tohoku.ac.jp

M. Itoh, K. Izawa, M. Kawai  
Fuji Silysia Chemical Ltd.  
2-1846 Kozoji-cho, Kasugai, Aichi 487-0013, Japan  
R. Crespo-Otero  
Department of Chemistry  
University College London  
2020 Gordon St., London WC1H 0AJ, UK

active carbon species; and iv) epitaxial growth and coalescence of the graphene nuclei.<sup>[13]</sup> Understanding the mechanism of these four steps is crucial as they determine the quality and uniformity of the resulting graphene material.<sup>[13b]</sup> It has been demonstrated that the kinetics of these four steps is greatly influenced by the catalytic properties of the template.<sup>[14]</sup> For instance, the activation of the C–H bonds determines the population of carbon active species, influences the growth kinetics, and affects the crystallinity of the fabricated graphene.<sup>[13b,15]</sup> Additionally, catalytic activity directly affects the reaction temperature,<sup>[16]</sup> residence time of precursor molecules and intermediate species,<sup>[17]</sup> and graphene growth rate,<sup>[18]</sup> ultimately determining the quality of the resulting graphene. Several studies have successfully used nano-porous Ni and Cu templates with high catalytic activity to fabricate highly crystalline graphene-based materials.<sup>[19]</sup> However, very few existing methods allow for control over the nanoporosity of the resulting material. This is because metal templates typically have low sintering temperatures, which often leads to the collapse of the nanostructures at the CVD temperature.

Alternative templates with better thermal stability include metal oxides, such as MgO,<sup>[20]</sup> Al<sub>2</sub>O<sub>3</sub>,<sup>[21]</sup> and CaO.<sup>[22]</sup> However, structural versatility of metal oxides is limited from the processing difficulties, thereby offering limited control on the resulting graphene-based materials. In this regard, SiO<sub>2</sub> is of particular interest owing to its diverse nano-structural controllability and bulk morphology.<sup>[23]</sup> CVD growth of carbon layers on SiO<sub>2</sub> templates potentially enables the production of graphene-based materials with a wide range of pre-designed morphologies. Nevertheless, the fabrication of high-quality graphene sheets on an SiO<sub>2</sub> surface via CVD remains challenging due to its low degree of catalytic activity toward hydrocarbon decomposition and the limited mobility of the carbon active species on the SiO<sub>2</sub> surface. The lack of catalytic activity tends to trigger competing gas-phase reactions involving a series of thermal decomposition and condensation reactions, resulting in the formation of large carbon species, or clusters.<sup>[24]</sup> Subsequent adsorption of these carbons on the solid surface may trigger the nucleation of amorphous carbon, which then undergoes lateral growth of soot-like carbon.<sup>[25]</sup> Additionally, the mobility limitation of active species induced by the oxygen-enriched SiO<sub>2</sub> surface is another hurdle. In particular, the cleaved hydrocarbon molecules may strongly interact with the oxygen sites on the SiO<sub>2</sub> surface, increasing nucleation density, and promoting the formation of grain boundary-rich (defect-rich) graphene.<sup>[26]</sup> Several techniques have been developed to overcome these challenges and realize a uniform graphene coating on SiO<sub>2</sub> templates, including the manipulation of CVD conditions (metal catalyst-introduction,<sup>[27]</sup> plasma-enhancement,<sup>[28]</sup> and CO<sub>2</sub> enhancement<sup>[29]</sup>), and surface silylation modification of the SiO<sub>2</sub> surface.<sup>[24]</sup> Due to its scalability, the latter method exhibits a remarkable advantage.<sup>[24]</sup>

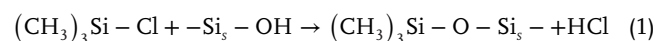
Trimethylsilylation has been reported to significantly enhance pyrolytic carbon deposition on SiO<sub>2</sub> during acetylene CVD (C<sub>2</sub>H<sub>2</sub>-CVD) at 600 °C.<sup>[24a]</sup> However, using such an unsaturated hydrocarbon with low dissociation energies as the precursor gas often causes complex reactions in the gas phase, leading to the formation of carbon coatings with high defect density and low crystallinity.<sup>[30]</sup> For example, C<sub>2</sub>H<sub>2</sub> can undergo a homogeneous pyrolysis reaction, resulting in the formation of long chain hy-

drocarbons (C<sub>4</sub>H<sub>4</sub>, C<sub>2</sub>H<sub>4</sub>, C<sub>2</sub>H<sub>6</sub>, and C<sub>6</sub>H<sub>6</sub>),<sup>[31]</sup> as well as polycyclic aromatic hydrocarbons (PAHs),<sup>[32]</sup> which can induce the growth of amorphous carbon, as mentioned before. The occurrence of these undesirable homogenous reactions can be avoided by utilizing a more thermodynamically stable carbon precursor gas, such as methane (CH<sub>4</sub>).<sup>[13a]</sup> Moreover, as the smallest hydrocarbon, CH<sub>4</sub> molecules exhibit high diffusivity into porous templates.<sup>[33]</sup> This can promote the uniform carbon coating onto small pore walls. Thus, the fabrication of graphene frameworks with higher quality than the unsaturated hydrocarbon counterparts is highly expected.

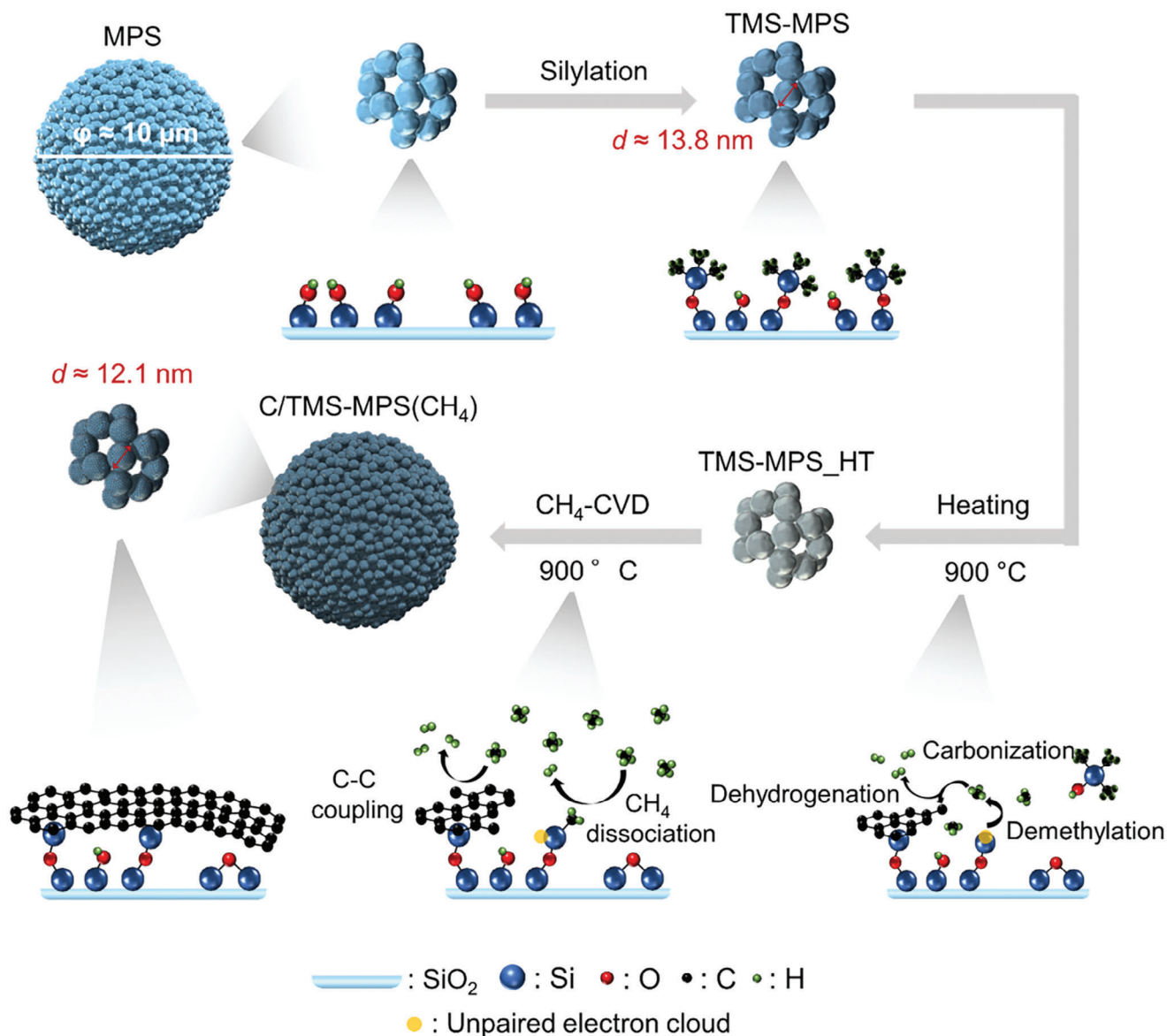
In this study, we report controlled graphene growth via (CH<sub>4</sub>-CVD) using trimethylsilyl functionalized micro-spherical porous silica (TMS-MPS) as the core material and examine the underlying reaction mechanism. Our results reveal that TMS groups on the SiO<sub>2</sub> surface evolve into silicon (Si) radicals and PAHs during the heating process of CVD (**Scheme 1**). The presence of Si radicals enhances carbon deposition significantly and reduces the onset temperature for graphene formation from 885 °C on pristine SiO<sub>2</sub> to 720 °C. Density functional theory (DFT) calculations suggest that Si radicals function as active sites for CH<sub>4</sub> dissociation, as well as promoters for further growth of second and third layers of graphene on the SiO<sub>2</sub> surface. This catalyst design utilizing TMS-MPS favors heterogeneous CH<sub>4</sub> decomposition, offering a more efficient and effective pathway for the synthesis of a high-quality graphene layer on the SiO<sub>2</sub> surface, which imparts the composite a high electrical conductivity of 0.25 S cm<sup>-1</sup>. This value surpasses that of a counterpart sample prepared via C<sub>2</sub>H<sub>2</sub>-CVD by a factor of ≈640 times, demonstrating the great advantage of the above methodology. Moreover, the isolated graphene framework has intactly replicated the micromorphology of the SiO<sub>2</sub> template on both the micro- and nano- levels. Our study furthers the understanding of graphene growth chemistries on a TMS-MPS surface and establishes a practically viable way in achieving nanoporous graphene frameworks with tunable microstructures and porosity.

## 2. Results and Discussion

Carbon deposition via CH<sub>4</sub>-CVD on TMS-MPS (provided by FUJI SILYSIA CHEMICAL Ltd.) is reported in this section. TMS-MPS is utilized in the form of spherical particles with an average diameter of 10 μm (Figures S1 and S2, Supporting Information) and the average nanopore size determined to be 13.8 nm (Figure S3, Supporting Information). TMS-MPS is prepared by mixing pristine MPS with trimethylsilyl chloride in toluene and heating it to 120 °C (Scheme 1). Under this condition, trimethylsilyl chloride acts as the silane coupling reagent, reacting with the surface silanol group, (-Si<sub>s</sub>-OH), as given by the following Equation 1.<sup>[34]</sup>



The functionalization on the MPS surface with TMS groups was verified via Fourier transform infrared (FTIR) spectroscopy, as depicted in **Figure 1a**. The presence of absorbance bands at ≈800 and 1107 cm<sup>-1</sup> in the spectra of MPS and TMS-MPS is attributed to the bending and asymmetric stretching vibrations of Si–O–Si bonds in the siliceous framework structure, respectively.<sup>[35]</sup> The absorbance at 970 cm<sup>-1</sup> and the broad peak



**Scheme 1.** Trimethylsilylation of the MPS template (top) and modification of the surface chemistry during each step of graphene coating process via  $\text{CH}_4$ -CVD (bottom). The  $\varphi$  and  $d$  denote the diameter and pore size of samples, respectively.

center  $\approx 3435 \text{ cm}^{-1}$  in the MPS spectrum correspond to the vibration of Si—OH bonds and OH stretching, respectively.<sup>[35,36]</sup> These characteristic bands of silanol groups are much less intense in the spectrum of TMS-MPS, as O—H bonds are ruptured due to the nucleophilic substitution reaction, as given by Equation 1. The presence of TMS groups on the TMS-MPS surface is corroborated by the occurrence of peaks assigned to the rocking vibration of  $\text{Si}(\text{CH}_3)_3$  at  $760 \text{ cm}^{-1}$ , the vibration of Si—CH<sub>3</sub> at  $846 \text{ cm}^{-1}$ , and the asymmetric C—H stretching at  $2964 \text{ cm}^{-1}$ .<sup>[37]</sup> The above results indicate the successful functionalization of the MPS surface with TMS groups, which is also supported by nuclear magnetic resonance (NMR) and Raman spectroscopy (Figure S4, Supporting Information). The TMS density in TMS-MPS is determined to be  $\approx 2.05 \text{ pcs nm}^{-2}$  using elemental analysis (Table S1, Supporting Information).

In this study, CVD is carried out at a temperature of  $900 \text{ }^\circ\text{C}$  (Scheme 1). Before introducing  $\text{CH}_4$  to trigger the carbon growth via CVD, TMS-MPS is stabilized at  $900 \text{ }^\circ\text{C}$  for 30 min (denoted TMS-MPS\_HT). The in situ weight change and gas evolution during the heating of the pristine MPS and TMS-MPS are observed using thermogravimetry (TG) coupled with mass spectroscopy (MS). The TG profile of MPS in Figure S5 (Supporting Information) exhibits weight loss upon heating due to  $\text{H}_2\text{O}$  desorption ( $m/z = 18$ ), corresponding to physically bound  $\text{H}_2\text{O}$  and dehydration reactions between silanol groups ( $>200 \text{ }^\circ\text{C}$ ) according to Equation 2.<sup>[38]</sup> In contrast, TMS-MPS shows little weight change from water loss upon heating (Figure 1b), which is in agreement with the FTIR results. In addition, the detected signal of  $m/z = 75$  at temperatures exceeding  $300 \text{ }^\circ\text{C}$  can be ascribed to a typical fragment of hydroxylated TMS, i.e.,  $(\text{CH}_3)_2$

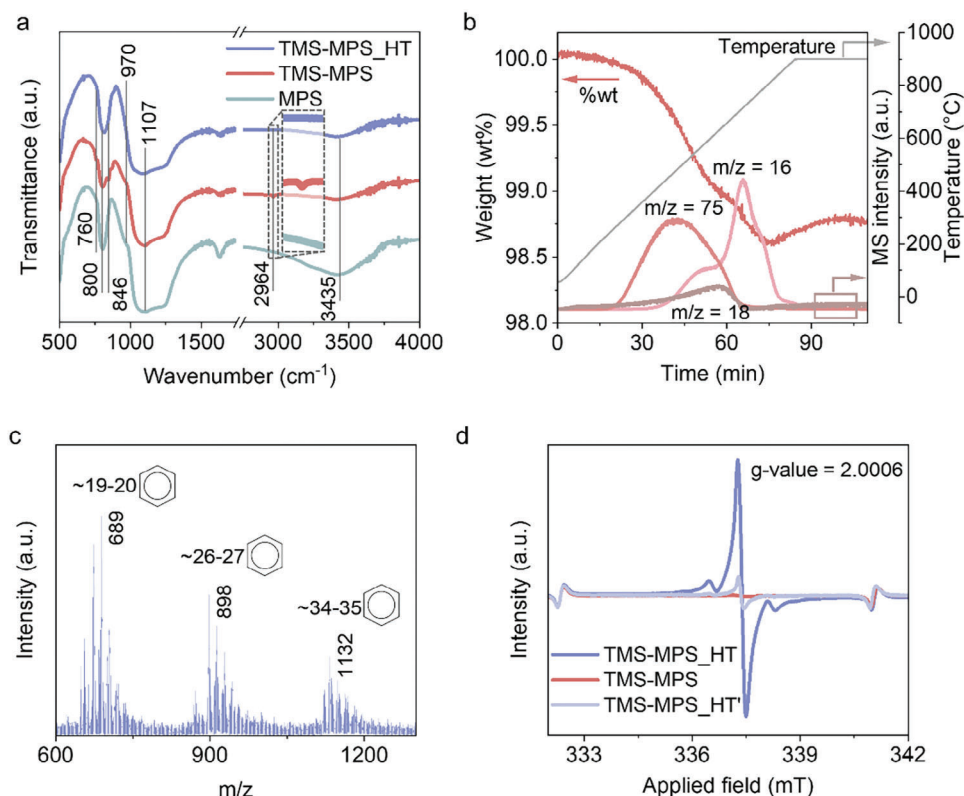
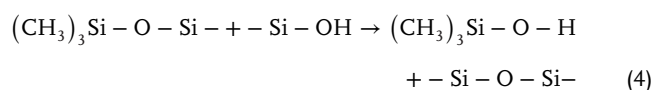
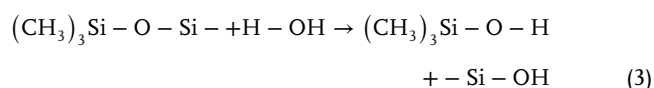
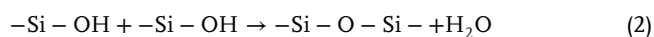


**Figure 1.** Changes in surface chemistry of SiO<sub>2</sub> materials used in this study. a) FTIR spectra of MPS, TMS-MPS, and TMS-MPS annealed at 900 °C for 30 min (TMS-MPS\_HT). The inset shows the enlarged spectra ranging from 2900 to 3020 cm<sup>-1</sup>. b) Gas evolution pattern and weight change during heating of TMS-MPS evaluated by TG-MS. c) MALDI-TOF-MS spectrum of carbonaceous species in TMS-MPS\_HT. The m/z values of the three peaks (689, 898, and 1132) are indicated, together with the number of benzene rings in the corresponding polyaromatic compounds. d) The ESR spectra of TMS-MPS and its derivatives.

Si-OH<sup>+</sup>), as TMS groups on TMS-MPS can react with desorbed H<sub>2</sub>O (Equation 3) or remaining hydroxyl groups (Equation 4).<sup>[39]</sup> Further, the detection of a signal of m/z = 16 (corresponding to CH<sub>4</sub><sup>+</sup> ions) after heating TMS-MPS to 400 °C suggests that TMS groups have undergone thermal demethylation. This is further confirmed from the later shown electron spin resonance (ESR) results. The detached methyl groups were likely to exist initially in a radical state, stabilized by hydrogen abstraction during transfer to a mass spectrometer.<sup>[24a]</sup> The signal of m/z = 16 disappears when the temperature reaches 900 °C, indicating the completion of demethylation. This result is in accordance with the FTIR spectrum of TMS-MPS heated at 900 °C for 30 min (TMS-MPS\_HT), where the absorbance band at 2964 cm<sup>-1</sup> that represents the C–H stretching is no longer visible (Figure 1a).



The evolution of these gases during the heating of TMS-MPS contributes to a weight loss of 1.29 wt.% (Figure 1b). This value is in line with the elemental analysis results, where TMS-MPS and TMS-MPS\_HT exhibit carbon contents of 1.88 % and 0.57 wt.%, respectively (Table S1, Supporting Information). The remaining carbonaceous species in the TMS-MPS\_HT are analyzed by matrix-assisted laser desorption/ionization-time of flight mass spectrometry (MALDI-TOF-MS), revealing peaks in the m/z values near 689, 898, and 1132 (Figure 1c). These compounds are likely PAHs, considering their thermodynamic stability at the given temperature,<sup>[40]</sup> and the absence of peaks corresponding to C–H bonding in the FTIR spectra (Figure 1a). In addition, the Raman spectrum of TMS-MPS\_HT exhibits broad and intense fluorescence bands (Figure S6, Supporting Information), indicating the existence of PAHs.<sup>[41]</sup> Figure 1d includes the ESR spectrum of TMS-MPS\_HT with showing triplet resonance with two pairs of satellites and a g value of 2.0006, suggesting the presence of Si radicals on TMS-MPS\_HT.<sup>[42]</sup> Since the pristine TMS-MPS presents no unpaired electrons from the ESR spectrum (Figure 1d), the Si radicals should have been formed from the splitting of methyl groups off the surface TMS groups. Moreover, the intensity of the resonance peaks in TMS-MPS\_HT after exposure to air for 3 weeks (denoted TMS-MPS\_HT') is significantly reduced because of the annihilation of Si radicals. Overall, the heating of TMS-MPS involves complicated detachment,

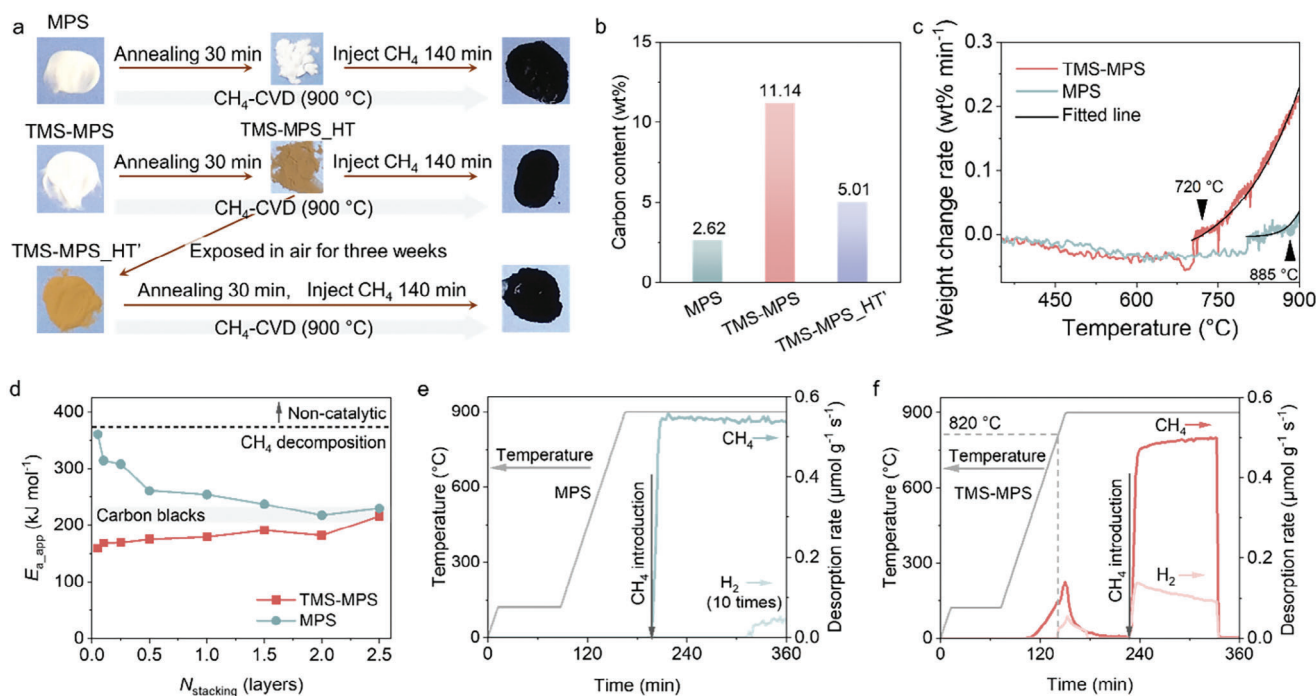


**Figure 2.** Carbon deposition behavior during  $\text{CH}_4$ -CVD. a) Optical images of the samples derived from MPS and TMS-MPS. b) Amounts of carbon deposited on templates after  $\text{CH}_4$ -CVD at  $900^\circ\text{C}$  for 140 min evaluated using TG analysis in air. c) The weight change of MPS and TMS-MPS monitored via in situ CVD-TG as the temperature is gradually increased in the presence of in-flowing  $\text{CH}_4$ . d) The dependence of  $E_{a,\text{app}}$  on  $N_{\text{stacking}}$ . e, f) The gas evolution patterns during  $\text{CH}_4$ -CVD using e) MPS and f) TMS-MPS as a template measured via in situ CVD-GC.

decomposition, and carbonization reactions, which lead to the formation of Si radicals and PAHs (Scheme 1). Notably, the scanning electron microscopy and atomic force microscopy of TMS-MPS and TMS-MPS\_HT' do not reveal visible differences in the microscopic and surface morphologies (Figures S1 and S7, Supporting Information). This suggests that PAHs are thin films that are tightly attached onto the  $\text{SiO}_2$  surface, which also accords well with the comparable nanopore size of TMS-MPS and TMS-MPS\_HT' (Figure S3, Supporting Information).

The formation of PAHs is consistent with the color change from white (TMS-MPS) to brown (TMS-MPS\_HT'). In contrast, MPS remains white after the annealing step, as shown in Figure 2a. To gain a better understanding of the influence of Si radicals and PAHs,  $\text{CH}_4$ -CVD is performed using three different templates: MPS (bare  $\text{SiO}_2$ ), TMS-MPS (with evolved Si radicals and PAHs), and TMS-MPS\_HT' (with evolved PAHs). As shown in Figure 2b, the carbon loading amount for MPS, TMS-MPS, and TMS-MPS\_HT' after  $\text{CH}_4$ -CVD at  $900^\circ\text{C}$  for 140 min are 2.62, 11.14, and 5.01 wt.%, respectively. Remarkably, the carbon deposition amount on the TMS-MPS is five times that corresponding to MPS, indicating significantly increased catalytic effect enhancement induced by Si radicals. The Si radical amount, which is positively correlated to the TMS group density, was found to show a positive correlation to the carbon deposition amount (Figure S8, Supporting Information). Since TMS-MPS\_HT' contains significantly fewer Si radicals compared to TMS-MPS\_HT' (Figure 1d), the carbon loading amount is correspondingly lower. Nevertheless, TMS-MPS\_HT' show a carbon deposition amount of nearly two times higher than that of the

MPS (Figure 2b), suggesting that PAHs also enhance the carbon deposition process. Indeed, edge sites of PAHs are known to act as nucleation sites and facilitate epitaxial growth during the subsequent carbonization process.<sup>[14,26,43]</sup>

Figure 2c shows the results of the in situ TG measurement during CVD (CVD-TG), where the onset temperature for carbon deposition is found to be  $885^\circ\text{C}$  for MPS. By contrast, the onset temperature for TMS-MPS is significantly lower as ca.  $720^\circ\text{C}$ . This can be ascribed to the enhancement coming from the thermally developed Si radicals and PAHs. The carbon deposition rate on as-prepared templates was further evaluated by monitoring the weight change during CVD, with the temperature maintained constant (Figure S9a, Supporting Information). As a result, TMS-MPS exhibited an average carbon deposition rate of  $3.48 \times 10^{-3} \text{ g}_{\text{carbon}} \text{ g}_{\text{template}}^{-1} \text{ min}^{-1}$  during the first 10 min of  $\text{CH}_4$ -CVD reaction, which is significantly higher than the  $1.10 \times 10^{-4} \text{ g}_{\text{carbon}} \text{ g}_{\text{template}}^{-1} \text{ min}^{-1}$  observed on pristine MPS (Figure S9b, Supporting Information). For a more straightforward understanding on the intrinsic differences, the apparent activation energy of carbon deposition reactions (denoted  $E_{a,\text{app}}$ ) is calculated according to the Arrhenius relationship (Detailed calculation is provided in Figure S10, Supporting Information). The  $E_{a,\text{app}}$  essentially reflects the activation energy of the  $\text{CH}_4$  decomposition reactions.<sup>[24a,44]</sup>

Figure 2d depicts the evolution of the  $E_{a,\text{app}}$  value as the average number of graphene layers stacked onto the template ( $N_{\text{stacking}}$ ) is gradually increased. In the case of MPS, the initial value of  $E_{a,\text{app}}$  ( $360 \text{ kJ mol}^{-1}$ ) is comparable to that of  $\text{CH}_4$  decomposition without a catalyst ( $370\text{--}433 \text{ kJ mol}^{-1}$ ),<sup>[45]</sup> highlighting

the inert nature of the SiO<sub>2</sub> surface with respect to superficial siloxane groups. Following the generation of graphene nuclei, the carbon deposition rate increases due to the potential C—C coupling reactions around the edges (Figure S10, Supporting Information), which in turn reduces  $E_{a,app}$ . Thus,  $E_{a,app}$  tends to decrease as carbon is deposited, becoming comparable to carbon growth on carbon blacks (205–236 kJ mol<sup>-1</sup>)<sup>[46]</sup> once the entire MPS surface is covered. On the other hand, the initial  $E_{a,app}$  for TMS-MPS is 130 kJ mol<sup>-1</sup>, which is significantly lower than that of MPS and carbon blacks. While PAHs triggers epitaxial graphene growth that resembles carbon blacks, the notably low initial  $E_{a,app}$  value undercores the predominant role of Si radicals in catalyzing the CH<sub>4</sub> dissociation reactions. This influence of Si radicals significantly overshadows the effects of PAHs. As the graphene growth further proceeds, the  $E_{a,app}$  value gradually increases, which is ascribed to the gradual poisoning effect as more graphene domains are formed.<sup>[47]</sup> Interestingly,  $E_{a,app}$  remains lower than that on carbon blacks even after the formation of the first graphene layer, which is in sharp contrast to the case of pristine MPS or metal oxide (including Al<sub>2</sub>O<sub>3</sub> and MgO),<sup>[44b]</sup> where  $E_{a,app}$  quickly reaches levels comparable to that on the carbon blacks. This suggests a different mechanism of nucleation and growth, where Si radicals facilitate the graphene growth continuously. The  $E_{a,app}$  of TMS-MPS eventually reaches a comparable level to that of carbon black after the  $N_{stacking}$  becomes  $\approx 2.5$  layers.

We also performed in situ gas chromatography analysis during the CVD process (CVD-GC) to monitor the gas emission behaviors for MPS and TMS-MPS templates. As shown in Figure 2e, MPS template shows no apparent gas emissions as it is gradually heated up to 900 °C. After the introduction of CH<sub>4</sub> into the system, the emission of H<sub>2</sub> at a rate of 0.003  $\mu\text{mol g}^{-1} \text{s}^{-1}$  was detected after an induction period of ca. 120 min. The formation of H<sub>2</sub> typically follows a pyrolytic decomposition reaction as simplified and shown in Equation 5.<sup>[44b]</sup>



By a sharp contrast, the TMS-MPS template was found to release CH<sub>4</sub> molecules as the temperature reaches 400 °C, which is in accordance with the TG-MS results (Figure 1b). In addition, H<sub>2</sub> emission was detected at a temperature of 820 °C. This should be from the conversion reactions of the in situ released CH<sub>4</sub> molecules into C species (Equation 5),<sup>[44]</sup> which has led to the formation of the above mentioned PAHs detected in TMS-MPS-HT. Moreover, immediately after the introduction of CH<sub>4</sub> into the system, a much more significant amount of H<sub>2</sub> was released at a rate of 0.1  $\mu\text{mol g}^{-1} \text{s}^{-1}$ . This clearly demonstrates the great enhancement of the CH<sub>4</sub> dissociation reactions with the utilization of the TMS-MPS template. It should be emphasized that no signal corresponding to CO evolution is detected on both MPS and TMS-MPS, indicating that oxygen-vacancy sites were not formed in these systems. This is different from metal oxides, such as Al<sub>2</sub>O<sub>3</sub> and MgO,<sup>[44]</sup> and where vacancy sites are formed to further catalyze the CH<sub>4</sub> decomposition reactions.<sup>[44]</sup>

DFT calculations were conducted to elucidate the experimental findings, particularly the role of Si radicals in enhancing carbon deposition. Initially, we constructed a model of an annealed amorphous SiO<sub>2</sub> template using ab initio molecular dynamics simu-

lations. Subsequently, we segmented the optimized bulk structure to create a surface containing a reactive center for the initial C—H activation reaction involving a three-coordinate Si and a one-coordinate Si (Figure S11, Supporting Information). The former represents the reactive site on the siloxane surface of the annealed MPS template, while the latter serves as a model for the Si radical generated through heat treatment of the TMS-MPS template. The energy profiles of CH<sub>4</sub> dissociation on annealed templates are depicted in Figure 3. The figure reveals that CH<sub>4</sub> adsorbs more strongly onto the three-coordinate Si of the MPSfa template, as evidenced by the higher adsorption energy ( $E_{ad} = -0.59$  eV) compared to the adsorption on the Si radical ( $E_{ad} = -0.17$  eV). As shown in Figure S12 (Supporting Information), CH<sub>4</sub> binds more strongly to the three-coordinate Si atom (Si<sub>3c</sub>) than to the one-coordinate Si atom (Si<sub>1c</sub>) because of its higher Bader charge and because CH<sub>4</sub> interacts with both the Si<sub>1c</sub> and Si<sub>4c</sub> atoms on the surface, resulting in a weaker interaction compared to Si<sub>3c</sub>. Nevertheless, the values are within reported the range of CH<sub>4</sub> adsorption on the SiO<sub>2</sub> surface computed by Zhao et al.<sup>[48]</sup> using the same level of theory as in our study. The subsequent dissociation of CH<sub>4</sub> into a surface-bound methyl group (CH<sub>3</sub><sup>\*</sup>) and a hydrogen atom (H<sup>\*</sup>) occurs via a transition state 1 (TS1). Notably, the Si radical exhibits a much lower activation energy of 0.32 eV for TS1, whereas the three-coordinate Si requires 1.74 eV. Following the formation of the CH<sub>3</sub><sup>\*</sup> state from TS1, both cases involve an energy dissipation step, resulting in energy decreases of 0.02 and 3.68 eV for TMS-MPS and MPS, respectively. Importantly, in the subsequent dehydrogenation step (Equation 6), the MPS surface necessitates a significant activation energy of 5.39 eV to reach transition state 2 (TS2).



Consequently, CH<sub>3</sub><sup>\*</sup> is likely to be strongly adsorbed and poison the three-coordinate Si site, preventing further C—H activation and hindering graphene growth. On the other hand, CH<sub>3</sub><sup>\*</sup> dissociation on the surface involving a Si radical is kinetically favorable with a lower barrier energy of 2.03 eV. However, the barrier for breaking the second C—H bond (CH<sub>3</sub>-to-CH<sub>2</sub>) is much higher than the first C—H bond (CH<sub>4</sub>-to-CH<sub>3</sub>), activation energy of 0.32 eV because it is accompanied by a larger charge redistribution, as shown in Figure S13 (Supporting Information). The resulting CH<sub>2</sub><sup>\*</sup> can be further dehydrogenated or act as the reactive intermediate for C—C coupling, promoting carbon growth.<sup>[49]</sup> Calculations were also conducted to determine the activation of CH<sub>4</sub> on two-coordinate Si species (Figure S14, Supporting Information), with the results showing much higher barriers than those obtained for the one- and three-coordinated Si species in Figure 3. These results reveal the possible mechanism of CH<sub>4</sub> dissociation, which is a typical rate-limiting step in graphene growth on SiO<sub>2</sub> surface during CH<sub>4</sub>-CVD, and confirm the role of Si radicals in catalyzing CH<sub>4</sub> activation, forming active carbon species. The formation of graphene nuclei is likely to be followed up by the coupling reactions of those active carbon species.<sup>[13d]</sup> The above observations support the notion that TMS-MPS exhibits a higher catalytic effect on carbon deposition compared to TMS-MPS-HT. Hence, the density of Si radicals is strongly correlated with the density of nucleation sites, which subsequently influences the density of grain-boundary defective sites.

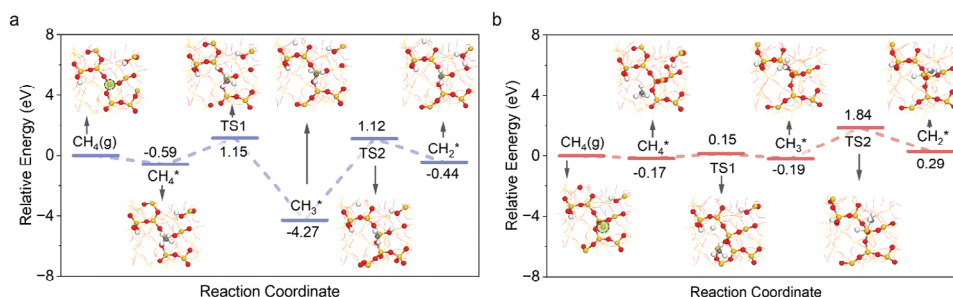


**Figure 3.** The energy profile of  $\text{CH}_4$  activation till the production of  $\text{CH}_2^*$  on a) the three-coordinate Si (representative of MPS template) and b) the one-coordinate Si (representative of TMS-MPS template). The asterisk (\*) denotes the adsorption state at the reaction site. The red, grey, purple, and white balls denote O, C, Si, and H atoms, respectively. The green areas indicate the reaction center sites.

Consequently, by utilizing  $\text{SiO}_2$  templates and adjusting the amounts of Si radicals, it becomes possible to exert control over the graphene growth process and manipulate the properties of the resulting carbon material. For instance, reducing the degree of trimethylsilylation can decrease the amount of Si radicals. Additionally, pre-calcining the pristine  $\text{SiO}_2$  template at a low temperature before trimethylsilylation would enhance the quantity of Si radicals. This step reduces the residual hydroxyl groups on TMS- $\text{SiO}_2$  template, thereby mitigating the potential for TMS detachment reaction during heating, as shown in Equations 3 and 4. As a result, more Si radicals are retained before the introduction of  $\text{CH}_4$ . In this regard, the optimization of Si radical amounts is imperative, as excessive nucleation sites can lead to a higher number of graphene boundaries, potentially compromising the crystallinity of the material.

In addition to the initial  $\text{CH}_4$  dissociation process, the influence of Si radicals on the multi-graphene layer formation was also investigated. **Figure 4** depicts the differences between the charge density at the interface of graphene configurations (consisting of one, two, and three graphene layers) induced by the presence of underlying Si radicals. As evident, the underlying Si radical induces electron dislocation on the surface graphene layer, leading to the formation of electron-rich and electron-deficient regions on the graphene layer. As shown in Figure 4, the yellow and blue regions represent electron-rich and electron-deficient regions, respectively. These regions are inclined to donate/accept electrons and potentially function as Lewis base and acid sites during the CVD process.<sup>[50]</sup> Since  $\text{CH}_4$  dissociation commonly oc-

urs through heterolytic bond cleavage, which typically involves the Lewis acid-base mechanism,<sup>[51]</sup> the Si radical-induced Lewis base and acid sites on the graphene layer can potentially catalyze the dissociation of  $\text{CH}_4$ . This is achieved by facilitating the transfer of protons between the acid and base, thereby promoting the reaction. Therefore, Si radicals have the potential to enhance carbon deposition on the top graphene layer. However, this influence gradually diminishes as additional graphene layers are stacked onto the initial layer, with the charge density distribution of the third graphene layer remaining nearly constant. These observations are consistent with the  $E_{a\_app}$  results, as depicted in Figure 2d.

The favorable reaction kinetics of the saturated  $\text{CH}_4$  molecules on Si radicals paves the path in achieving graphene frameworks with a low defect density and high crystallinity. TMS-MPS was successfully coated with pseudo-single layer graphene building blocks via  $\text{CH}_4$ -CVD (Figure S15, Supporting Information). The resulting composite, denoted as C/TMS-MPS( $\text{CH}_4$ ), displays slight increase in the specific surface area compared to the template (Figure S3, Supporting Information), which is likely to be contributed by the carbon edge sites.<sup>[52]</sup> **Figure 5a** presents the Raman spectrum of this composite. In the spectrum, the D, A, and G bands are evident, with the G-band representing the stretching vibrations of  $\text{sp}^2$  hybridized carbon atoms within the graphene structure. The D and A bands, on the other hand, correspond to defect sites within the graphene lattice. The D band is particularly sensitive to disorder within the  $\text{sp}^2$  carbon network, while the A band is indicative of the presence of  $\text{sp}^3$

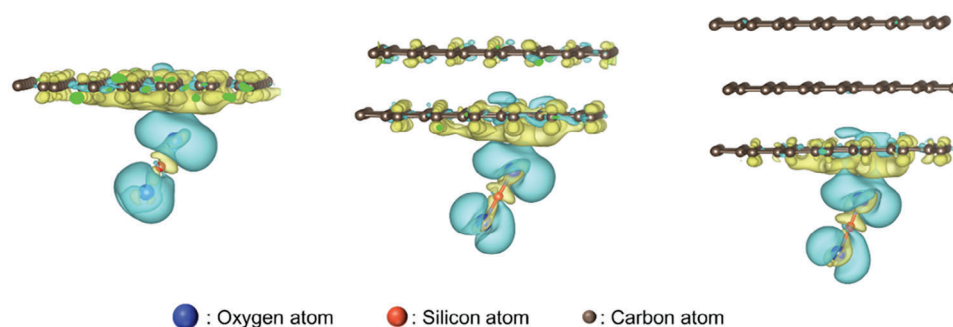


**Figure 4.** Charge density mappings of graphene/Si radical systems containing one graphene layer (left), two graphene layers (middle), and three graphene layers (right) over one Si radical. The yellow and blue regions represent areas with an increase and decrease in charge densities, respectively, compared with the counterpart systems involving no Si radicals.

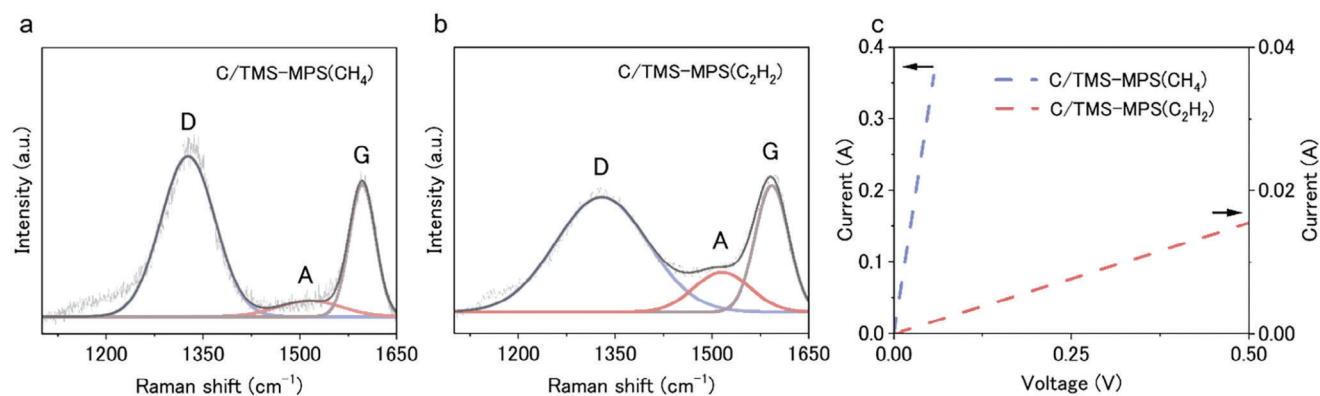


**Figure 5.** The Raman spectra of a) C/TMS-MPS(CH<sub>4</sub>) and b) C/TMS-MPS(C<sub>2</sub>H<sub>2</sub>), where deconvolution method reported by Hu et al. was used.<sup>[13]</sup> c) The Current-Voltage (*I*-*V*) curve of C/TMS-MPS(CH<sub>4</sub>) and C/TMS-MPS(C<sub>2</sub>H<sub>2</sub>) under constant pressure of 6 MPa.

interstitial sites and non-hexagonal rings.<sup>[53]</sup> According to this, C/TMS-MPS(CH<sub>4</sub>) demonstrates characteristics of a highly crystalline graphene-based material, exhibiting a low ratio of the D band intensity and A band to that of the G band (referred to as  $I_D/I_G$ , and  $I_A/I_G$ , respectively), with respective values of 2.42 and 0.16 (Table S2, Supporting Information). However, counterpart composite prepared with an unsaturated carbon precursor, denoted C/TMS-MPS(C<sub>2</sub>H<sub>2</sub>), exhibits intensified and broadened D and A bands on Raman spectra (Figure 5b). These enhancements result in substantially higher  $I_D/I_G$ , and  $I_A/I_G$  values of 3.12 and 0.66, respectively (Table S2, Supporting Information), indicating a pronounced abundance of disordered structures within the carbon framework. The highly ordered sp<sup>2</sup> hybridized carbon structure presented in C/TMS-MPS(CH<sub>4</sub>) facilitates the establishment of  $\pi$ - $\pi$  conjugation,<sup>[54]</sup> thereby enhancing electron mobility and enabling an electrical conductivity of 0.25 S cm<sup>-1</sup> under a compression force of 6 MPa (Figure 5c). Conversely, the existence of defect sites that undermine crystallinity can lead to electron scattering and hinder their movement throughout the lattice.<sup>[55]</sup> C/TMS-MPS(C<sub>2</sub>H<sub>2</sub>), recognized as a highly defective graphene framework, exhibits a much lower electrical conductivity of  $3.9 \times 10^{-4}$  S cm<sup>-1</sup> under the same conditions (Figure 5c). Due to the presence of high crystallinity carbon, C/TMS-MPS(CH<sub>4</sub>) offers excellent affinity with electrochemical biosensors.<sup>[56]</sup>

One of the most notable advantages of the aforementioned methodology lies in its ability to establish a precise and controlled approach for obtaining carbons with predetermined microstructures. By removing the SiO<sub>2</sub> template from C/TMS-MPS(CH<sub>4</sub>), we have obtained a well-defined nanoporous graphene framework that mirrors the structural features of the parental TMS-MPS template (Figures S1–S3, Supporting Information). More importantly, the templated carbon, denoted TC(CH<sub>4</sub>), exhibits a large Brunauer–Emmett–Teller surface area of 1817 m<sup>2</sup> g<sup>-1</sup> (Figure S3, Supporting Information). This value suggests a highly exposed state of the graphene domains, which corresponds to an average stacking number of 1.1 (Figure S15, Supporting Information). The above assertion was further validated by XRD analysis, which revealed a broad 002 peak and sharp 10 peak, characteristic of graphene crystallites with a weakly stacked arrangement (Figure S16, Supporting Information). All the above results suggest that graphene has been uniformly

coated onto the TMS-MPS template via the CVD process, free from obvious aggregation. Since SiO<sub>2</sub> can be manufactured into a variety of different microstructures, our methodology offers a unique and promising approach for achieving nanoporous graphene frameworks with high crystallinity and pre-defined microstructures.

### 3. Conclusion

In this work, we demonstrate the successful formation of a high-quality graphene layer via CH<sub>4</sub>-CVD on TMS-modified SiO<sub>2</sub>. Our catalyst design leverages the thermal decomposition of TMS groups, which generates Si radicals and PAHs that act as potent catalysts for the CH<sub>4</sub>-to-C conversion reactions. This design significantly enhances the surface catalytic activity, making the graphene formation process thermodynamically favorable on TMS-MPS compared to MPS. It also reduces the reaction onset temperature from 885° to 720 °C. DFT calculations corroborate the catalytic effect of Si radicals on the CH<sub>4</sub> dissociation that facilitates graphene growth. The catalytic enhancement, combined with the utilization of CH<sub>4</sub>-CVD, offers the advantage of facilitating heterogeneous reactions on the surface of the TMS-MPS template, which results in the formation of high-quality graphene. The obtained graphene framework can be isolated from the template while preserving the replica structure of the parent template. These results underscore the effectiveness of our catalyst design in achieving graphene-based materials with high crystallinity and pre-designed nanoporous structures.

### Supporting Information

Supporting Information is available from the Wiley Online Library or from the author.

### Acknowledgements

K.P. and Q.Z. contributed equally to this work. This work was supported by the JST A-STEP (Grant no. JPMJTR22T6), the JST SICORP (Grant no. JPMJSC2112), and the UK's Royal Society International Exchanges Cost Share (IEC\R3\193106). The authors thank Koki Chida for supporting MALDI-TOF-MS measurements. Q.Z. thanks the China Scholarship Council for financial support. The authors are grateful to the UK Materials



and Molecular Modeling Hub for computational resources, which was partially funded by the EPSRC (EP/P020194/1). Via the membership of the UK's HEC Materials Chemistry Consortium, which was funded by the EPSRC (EP/L000202), this work used the ARCHER UK National Supercomputing Service (<https://www.archer.ac.uk>). This research utilized Queen Mary's Apocrita HPC facility, supported by QMUL Research-IT. <https://doi.org/10.5281/zenodo.438045>.

## Conflict of Interest

The authors declare no conflict of interest.

## Data Availability Statement

The data that support the findings of this study are available from the corresponding author upon reasonable request

## Keywords

chemical vapor deposition, CH<sub>4</sub> activation, carbon templating, graphene, silicon radical

Received: July 25, 2023  
Revised: November 5, 2023  
Published online:

- [1] a) L. Ren, K. N. Hui, K. S. Hui, Y. Liu, X. Qi, J. Zhong, Y. Du, J. Yang, *Sci. Rep.* **2015**, *5*, 14229; b) C. Xiong, B. Li, X. Lin, H. Liu, Y. Xu, J. Mao, C. Duan, T. Li, Y. Ni, *Composites, Part B* **2019**, *165*, 10; c) H. Jahandideh, J.-R. Macairan, A. Bahmani, M. Lapointe, N. Tufenkji, *Chem. Sci.* **2022**, *13*, 8924; d) G. Li, B. Huang, Z. Pan, X. Su, Z. Shao, L. An, *Energy Environ. Sci.* **2019**, *12*, 2030.
- [2] A. Ohma, Y. Furuya, T. Mashio, M. Ito, K. Nomura, T. Nagao, H. Nishihara, H. Jinnai, T. Kyotani, *Electrochim. Acta* **2021**, *370*, 137705.
- [3] K. Nomura, H. Nishihara, N. Kobayashi, T. Asada, T. Kyotani, *Energy Environ. Sci.* **2019**, *12*, 1542.
- [4] L. Lu, F. Pei, T. Abeln, Y. Pei, *Carbon* **2020**, *157*, 437.
- [5] W. Yu, T. Yoshii, A. Aziz, R. Tang, Z.-Z. Pan, K. Inoue, M. Kotani, H. Tanaka, E. Scholtzová, D. Tunega, Y. Nishina, K. Nishioka, S. Nakanishi, Y. Zhou, O. Terasaki, H. Nishihara, *Adv. Sci.*, *10*, 2300268.
- [6] a) M.-Q. Yang, N. Zhang, M. Pagliaro, Y.-J. Xu, *Chem. Soc. Rev.* **2014**, *43*, 8240; b) N. Zhang, M.-Q. Yang, S. Liu, Y. Sun, Y.-J. Xu, *Chem. Rev.* **2015**, *115*, 10307; c) C. Han, N. Zhang, Y.-J. Xu, *Nano Today* **2016**, *11*, 351; d) C. Han, Y.-H. Li, M.-Y. Qi, F. Zhang, Z.-R. Tang, Y.-J. Xu, *Sol. RRL* **2020**, *4*, 1900577.
- [7] T. Yoshii, D. Umemoto, M. Yamamoto, Y. Kuwahara, H. Nishihara, K. Mori, T. Kyotani, H. Yamashita, *ChemCatChem* **2020**, *12*, 5880.
- [8] K. Nomura, H. Nishihara, M. Yamamoto, A. Gabe, M. Ito, M. Uchimura, Y. Nishina, H. Tanaka, M. T. Miyahara, T. Kyotani, *Nat. Commun.* **2019**, *10*, 2559.
- [9] H. Nishihara, T. Simura, S. Kobayashi, K. Nomura, R. Berenguer, M. Ito, M. Uchimura, H. Iden, K. Arihara, A. Ohma, Y. Hayasaka, T. Kyotani, *Adv. Funct. Mater.* **2016**, *26*, 6418.
- [10] X. Wang, Y. Zhang, C. Zhi, X. Wang, D. Tang, Y. Xu, Q. Weng, X. Jiang, M. Mitome, D. Golberg, Y. Bando, *Nat. Commun.* **2013**, *4*, 2905.
- [11] a) X. Huang, K. Qian, J. Yang, J. Zhang, L. Li, C. Yu, D. Zhao, *Adv. Mater.* **2012**, *24*, 4419; b) Y. He, J. Li, K. Luo, L. Li, J. Chen, J. Li, *Ind. Eng. Chem. Res.* **2016**, *55*, 3775; c) M. A. Worsley, P. J. Pauzauskie, T. Y. Olson, J. Biener, J. H. Satcher, T. F. Baumann, *J. Am. Chem. Soc.* **2010**, *132*, 14067.
- [12] a) H.-J. Peng, J. Liang, L. Zhu, J.-Q. Huang, X.-B. Cheng, X. Guo, W. Ding, W. Zhu, Q. Zhang, *ACS Nano* **2014**, *8*, 11280; b) J.-L. Shi, C. Tang, H.-J. Peng, L. Zhu, X.-B. Cheng, J.-Q. Huang, W. Zhu, Q. Zhang, *Small* **2015**, *11*, 5243.
- [13] a) Z. Sun, S. Fang, Y. H. Hu, *Chem. Rev.* **2020**, *120*, 10336; b) L. Lin, B. Deng, J. Sun, H. Peng, Z. Liu, *Chem. Rev.* **2018**, *118*, 9281; c) L. Wang, R. Lai, L. Zhang, M. Zeng, L. Fu, *ACS Mater. Lett.* **2022**, *4*, 528; d) H. Cao, C. Wang, B. Li, T. Chen, P. Han, Y. Zhang, H. Yang, Q. Li, A. K. Cheetham, *CCS Chem.* **2022**, *4*, 584.
- [14] L. Wang, R. Lai, L. Zhang, M. Zeng, L. Fu, *ACS Mater. Lett.* **2022**, *4*, 528.
- [15] a) Z. Peng, Z. Yan, Z. Sun, J. M. Tour, *ACS Nano* **2011**, *5*, 8241; b) P. Wu, W. Zhang, Z. Li, J. Yang, *Small* **2014**, *10*, 2136; c) J. Gao, Q. Yuan, H. Hu, J. Zhao, F. Ding, *J. Phys. Chem.* **2011**, *115*, 17695; d) H. Kim, C. Mattevi, M. R. Calvo, J. C. Oberg, L. Artiglia, S. Agnoli, C. F. Hirjibehedin, M. Chhowalla, E. Saiz, *ACS Nano* **2012**, *6*, 3614; e) J. Gao, J. Yip, J. Zhao, B. I. Yakobson, F. Ding, *J. Am. Chem. Soc.* **2011**, *133*, 5009; f) H. Shu, X.-M. Tao, F. Ding, *Nanoscale* **2015**, *7*, 1627.
- [16] S. Meskinis, A. Vasiliauskas, A. Guobiene, M. Talaikis, G. Niaura, R. Gudaitis, *RSC Adv.* **2022**, *12*, 18759.
- [17] F. B. Fauzi, E. Ismail, S. N. Syed Abu Bakar, A. F. Ismail, M. A. Mohamed, M. F. Md Din, S. Ilias, M. H. Ani, *Phys. Chem. Chem. Phys.* **2020**, *22*, 3481.
- [18] H.-T. Chin, J.-J. Lee, M. Hofmann, Y.-P. Hsieh, *Sci. Rep.* **2018**, *8*, 4046.
- [19] a) Y. Ito, Y. Tanabe, H.-J. Qiu, K. Sugawara, S. Heguri, N. H. Tu, K. K. Huynh, T. Fujita, T. Takahashi, K. Tanigaki, M. Chen, *Angew. Chem., Int. Ed. Engl.* **2014**, *53*, 4822; b) L. Zhang, N. T. Alvarez, M. Zhang, M. Haase, R. Malik, D. Mast, V. Shanov, *Carbon* **2015**, *82*, 353; c) D. Dearmond, L. Zhang, R. Malik, K. Vamsi Krishna Reddy, N. T. Alvarez, M. R. Haase, Y.-Y. Hsieh, S. N. Kanakaraj, N. Oslin, J. Brunemann, J. Daum, V. Shanov, *Mater. Sci. Eng. B* **2020**, *254*, 114510.
- [20] G. Ning, Z. Fan, G. Wang, J. Gao, W. Qian, F. Wei, *Chem. Commun.* **2011**, *47*, 5976.
- [21] M. Zhou, T. Lin, F. Huang, Y. Zhong, Z. Wang, Y. Tang, H. Bi, D. Wan, J. Lin, *Adv. Funct. Mater.* **2013**, *23*, 2263.
- [22] C. Tang, B.-Q. Li, Q. Zhang, L. Zhu, H.-F. Wang, J.-L. Shi, F. Wei, *Adv. Funct. Mater.* **2016**, *26*, 577.
- [23] a) C. T. Kresge, W. J. Roth, *Chem. Soc. Rev.* **2013**, *42*, 3663; b) V. Zelenak, J. Magura, A. ZelenaKová, R. Smolková, *Pure Appl. Chem.* **2017**, *89*, 493; c) S.-D. Kim, S. Surabhi, J. Choi, J.-R. Jeong, *Electron. Mater. Lett.* **2019**, *15*, 673; d) M. Kosari, U. Anjum, S. Xi, A. M. H. Lim, A. M. Seayad, E. A. J. Raj, S. M. Kozlov, A. Borgna, H. C. Zeng, *Adv. Funct. Mater.* **2021**, *31*, 2102896; e) Y. Wu, P. Wang, C. Zhen, K. Zhang, W. Guo, X. Zhai, L. Ma, D. Hou, *J. Porous Mater.* **2018**, *25*, 23.
- [24] a) Y. Hoshikawa, A. Castro-Muñiz, H. Komiyama, T. Ishii, T. Yokoyama, H. Nanbu, T. Kyotani, *Carbon* **2014**, *67*, 156; b) A. M. Lewis, B. Derby, I. A. Kinloch, *ACS Nano* **2013**, *7*, 3104; c) Z. Li, W. Zhang, X. Fan, P. Wu, C. Zeng, Z. Li, X. Zhai, J. Yang, J. Hou, *J. Phys. Chem.* **2012**, *116*, 10557.
- [25] a) A. Shivayogimath, D. Mackenzie, B. Luo, O. Hansen, P. Bøggild, T. J. Booth, *Sci. Rep.* **2017**, *7*, 6183; b) K. Jia, H. Ci, J. Zhang, Z. Sun, Z. Ma, Y. Zhu, S. Liu, J. Liu, L. Sun, X. Liu, J. Sun, W. Yin, H. Peng, L. Lin, Z. Liu, *Angew. Chem., Int. Ed. Engl.* **2020**, *59*, 17214.
- [26] Z. Chen, Y. Qi, X. Chen, Y. F. Zhang, Z. Liu, *Adv. Mater.* **2019**, *31*, 1803639.
- [27] a) H. Kim, I. Song, C. Park, M. Son, M. Hong, Y. Kim, J. S. Kim, H.-J. Shin, J. Baik, H. C. Choi, *ACS Nano* **2013**, *7*, 6575; b) P.-Y. Teng, C.-C. Lu, K. Akiyama-Hasegawa, Y.-C. Lin, C.-H. Yeh, K. Suenaga, P.-W. Chiu, *Nano Lett.* **2012**, *12*, 1379; c) C.-Y. Su, A.-Y. Lu, C.-Y. Wu, Y.-T. Li, K.-K. Liu, W. Zhang, S.-Y. Lin, Z.-Y. Juang, Y.-L. Zhong, F.-R. Chen, L.-J. Li, *Nano Lett.* **2011**, *11*, 3612.
- [28] a) L. Zhang, Z. Shi, Y. Wang, R. Yang, D. Shi, G. Zhang, *Nano Res.* **2011**, *4*, 315; b) J. Sun, Y. Chen, X. Cai, B. Ma, Z. Chen, M. K. Priyadarshi, K. Chen, T. Gao, X. Song, Q. Ji, X. Guo, D. Zou, Y. Zhang,

- Z. Liu, *Nano Res.* **2015**, *8*, 3496; c) H. Ci, H. Ren, Y. Qi, X. Chen, Z. Chen, J. Zhang, Y. Zhang, Z. Liu, *Nano Res.* **2018**, *11*, 3106.
- [29] I. H. Son, J. H. Park, S. Kwon, J. W. Choi, M. H. Rummeli, *Small* **2016**, *12*, 658.
- [30] H. Abdullah, I. Ramli, I. Ismail, N. Yusof, *Pertanika J. Sci. Technol.* **2017**, *25*, 379.
- [31] a) D. Buchholz, R. U. Khan, S. Bajohr, R. Reimert, *Ind. Eng. Chem. Res.* **2010**, *49*, 1130; b) T. Mendiara, M. P. Domene, A. Millera, R. Bilbao, M. U. Alzueta, *J Anal Appl Pyrolysis* **2005**, *74*, 486.
- [32] H. Tao, H.-Y. Wang, W. Ren, K. C. Lin, *Fuel* **2019**, *255*, 115796.
- [33] a) B. R. Byron, S. E. Warren, L. N. Edwin, *Transport Phenomena*, John Wiley & Sons, Inc., New York, **2001**. b) S. Gruener, P. Huber, *Phys. Rev. Lett.* **2008**, *100*, 064502.
- [34] J. Duchoslav, A. Lumetzberger, D. Leidlmair, M. Kehrner, G. Säckl, S. Breitenbach, C. Unterweger, C. Fürst, D. Stifter, *Surf. Interfaces* **2021**, *23*, 100957.
- [35] S. Loganathan, M. Tikmani, A. K. Ghoshal, *Langmuir* **2013**, *29*, 3491.
- [36] C. S. Srikanth, S. S. C. Chuang, *J Phys Chem.* **2013**, *117*, 9196.
- [37] a) P. B. Sarawade, J.-K. Kim, H.-K. Kim, H.-T. Kim, *Appl. Surf. Sci.* **2007**, *254*, 574; b) C. Jiang, Y. Zhang, Q. Wang, T. Wang, *J. Appl. Polym. Sci.* **2013**, *129*, 2959.
- [38] B. Charmas, K. Kucio, V. Sydoruk, S. Khalameida, M. Ziezio, A. Nowicka, *Colloids Interfaces* **2018**, *3*, 6.
- [39] J. W. Severin, H. Van Der Wel, I. G. J. Camps, J. M. E. Baken, J. M. J. Vankan, *Surf. Interface Anal.* **1992**, *19*, 133.
- [40] J. Gao, Q. Yuan, H. Hu, J. Zhao, F. Ding, *J Phys Chem.* **2011**, *115*, 17695.
- [41] a) E. Cloutis, P. Szymanski, D. Applin, D. Goltz, *Icarus* **2016**, *274*, 211; b) N. Zhang, Z. Tian, Y. Leng, H. Wang, F. Song, J. Meng, *Sci. China, Ser. D: Earth Sci.* **2007**, *50*, 1171.
- [42] a) R. Kinjo, M. Ichinohe, A. Sekiguchi, *J. Am. Chem. Soc.* **2007**, *129*, 26; b) K. Chandra Mondal, S. Roy, H. W. Roesky, *Chem. Soc. Rev.* **2016**, *45*, 1080.
- [43] V. O. Özçelik, S. Cahangirov, S. Ciraci, *Phys. Rev. B* **2012**, *85*, 235456.
- [44] a) I. Vlasiouk, M. Regmi, P. Fulvio, S. Dai, P. Datskos, G. Eres, S. Smirnov, *ACS Nano* **2011**, *5*, 6069; b) S. Sunahiro, K. Nomura, S. Goto, K. Kanamaru, R. Tang, M. Yamamoto, T. Yoshii, J. N. Kondo, Q. Zhao, A. Ghulam Nabi, R. Crespo-Otero, D. Di Tommaso, T. Kyotani, H. Nishihara, *J Mater Chem.* **2021**, *9*, 14296.
- [45] A. Holmen, O. A. Rokstad, A. Solbakken, *Ind. Eng. Chem. Process Des. Dev.* **1976**, *15*, 439.
- [46] N. Muradov, F. Smith, A. T-Raissi, *Catal. Today* **2005**, *102–103*, 225.
- [47] R. Muñoz, C. Gómez-Aleixandre, *Chem. Vap. Deposition* **2013**, *19*, 297.
- [48] J. Zhao, Z. Wang, P. Guo, Q. Luo, *Comput. Mater. Sci.* **2019**, *168*, 213.
- [49] Q. Zhao, M. Yamamoto, K. Yamazaki, H. Nishihara, R. Crespo-Otero, D. Di Tommaso, *Phys. Chem. Chem. Phys.* **2022**, *24*, 23357.
- [50] K. Gupta, D. R. Roy, V. Subramanian, P. K. Chattaraj, *J. Mol. Struct.* **2007**, *812*, 13.
- [51] M. Yamamoto, Q. Zhao, S. Goto, Y. Gu, T. Toriyama, T. Yamamoto, H. Nishihara, A. Aziz, R. Crespo-Otero, D. Di Tommaso, M. Tamura, K. Tomishige, T. Kyotani, K. Yamazaki, *Chem. Sci.* **2022**, *13*, 3140.
- [52] a) K. Pirabul, Z.-Z. Pan, R. Tang, S. Sunahiro, H. Liu, K. Kanamaru, T. Yoshii, H. Nishihara, *Bull. Chem. Soc. Jpn.* **2023**, *96*, 510; b) T. Xia, T. Yoshii, K. Nomura, K. Wakabayashi, Z.-Z. Pan, T. Ishii, H. Tanaka, T. Mashio, J. Miyawaki, T. Otomo, K. Ikeda, Y. Sato, M. Terauchi, T. Kyotani, H. Nishihara, *Chem. Sci.* **2023**, *14*, 8448.
- [53] a) M. W. Smith, I. Dallmeyer, T. J. Johnson, C. S. Brauer, J.-S. Mcewen, J. F. Espinal, M. Garcia-Perez, *Carbon* **2016**, *100*, 678; b) C. Hu, S. Sedghi, A. Silvestre-Albero, G. G. Andersson, A. Sharma, P. Pendleton, F. Rodríguez-Reinoso, K. Kaneko, M. J. Biggs, *Carbon* **2015**, *85*, 147; c) C. Guizani, K. Haddad, L. Limousy, M. Jeguirim, *Carbon* **2017**, *119*, 519; d) X. Li, J. Hayashi, C. Li, *Fuel* **2006**, *85*, 1509; e) J. Xu, H. Tang, S. Su, J. Liu, K. Xu, K. Qian, Y. Wang, Y. Zhou, S. Hu, A. Zhang, J. Xiang, *Appl. Energy* **2018**, *212*, 46.
- [54] a) S. V. Morozov, K. S. Novoselov, M. I. Katsnelson, F. Schedin, D. C. Elias, J. A. Jaszczak, A. K. Geim, *Phys Rev Lett.* **2008**, *100*, 016602; b) K. I. Bolotin, K. J. Sikes, Z. Jiang, M. Klima, G. Fudenberg, J. Hone, P. Kim, H. L. Stormer, *Solid State Commun.* **2008**, *146*, 351.
- [55] F. Banhart, J. Kotakoski, A. V. Krasheninnikov, *ACS Nano* **2011**, *5*, 26.
- [56] S. Fujii, A. Yoshida, T. T. Chuong, Y. Minegishi, K. Pirabul, Z.-Z. Pan, Y. Nishina, T. Kyotani, H. Nishihara, K. Masumoto, G. D. Stucky, T. Itoh, *ACS Appl. Eng. Mater.* **2023**, *1*, 1426.